Acta Biomaterialia 97 (2019) 671–680

Contents lists available at ScienceDirect

Acta Biomaterialia

journal homepage: www.elsevier.com/locate/actabiomat

Full length article

A numerical corrosion-fatigue model for biodegradable Mg alloy stents

Zhenquan Shen [a], Ming Zhao [b], Xiaochen Zhou [a], Hongtao Yang [a], Jianing Liu [c], Hui Guo [a], Yufeng Zheng [a,c,*], Jian-An Yang [d,*]

[a] Beijing Advanced Innovation Center for Materials Genome Engineering & Department of Materials Science and Engineering, College of Engineering, Peking University, Beijing 100871, China
[b] Schlumberger Technology Corporation, Houston, TX 77054, USA
[c] Center for Biomedical Materials and Tissue Engineering, Academy for Advanced Interdisciplinary Studies, Peking University, Beijing 100871, China
[d] Department of Geriatrics and Cardiovascular Medicine, Shenzhen Sun Yat-Sen Cardiovascular Hospital, Shenzhen 518112, China

ARTICLE INFO

Article history:
Received 25 April 2019
Received in revised form 22 July 2019
Accepted 1 August 2019
Available online xxxx

Keywords:
Corrosion fatigue
Biodegradation
Magnesium alloys
Stent
Continuum damage mechanics
Finite element method

ABSTRACT

Biodegradable magnesium alloys have attracted research interest as matrix materials for next-generation absorbable metallic coronary stents. Subject to cyclic stresses, magnesium alloy stents (MAS) are prone to premature failures caused by corrosion fatigue damage. This work aimed to develop a numerical continuum damage mechanics model, implemented with the finite element method, which can account for the corrosion fatigue of Mg alloys and the applications in coronary stents. The parameters in the resulting phenomenological model were calibrated using our previous experimental data of HP-Mg and WE43 alloy and then applied in assessing the performance of the MAS. The results indicated that it was valid to predict the degradation rate, the damage-induced reduction of the radial stiffness, and the critical location of the MAS. Furthermore, this model and the numerical procedure can be easily adapted for other biodegradable alloy systems, for instance, Fe and Zn, and used to achieve the optimal degradation rate while improving fatigue endurance.

Statement of Significance

Subject to cyclic stresses, magnesium alloy stents are prone to premature failures caused by corrosion fatigue damage. This work aimed to develop a numerical continuum damage mechanics model, implemented with the finite element method, which can account for the corrosion fatigue of Mg alloys and the applications in coronary stents. The results indicated that it was valid to predict the degradation rate, damage-induced reduction of the radial stiffness, and the critical location of the Mg alloy stent; therefore, these stents can be easily adapted to other biodegradable alloy systems such as Fe and Zn.

1. Introduction

Magnesium (Mg) and its alloys have drawn increasing research attention in recent years as next-generation biomaterials owing to their biodegradable behaviors [1–4]. Mg alloys degrade by corrosion in the physiological environment into soluble and nontoxic by-products. Unlike the conventional structural materials, for which the vulnerability to corrosion is detrimental, the ability to be gradually degraded and eventually absorbed by the body makes Mg alloys favorable for biomedical applications [1]. One application extensively studied is the Mg alloy stents (MAS) used in coronary artery surgeries [2,5–8]. Coronary stents are small mesh-like tubular scaffolds that are placed into the coronary arteries immediately after the angioplasty procedure. The stent expands inside the artery and provides mechanical support to prevent the artery from closing up again, referred to as the elastic arterial recoil [9]. However, the need for mechanical support is temporary. Stents that are fabricated from biodegradable Mg alloys, in contrast to the permanent stents, are targeted to lose their mechanical support gradually by corrosion and degrade with time to allow blood vessel remodeling and growth [2,10–12], thus eliminating the need for a second surgery.

However, the time span for stent degradation does not always match well with the time required for arterial healing period, typically 3–4 months for the coronary artery as determined from

* Corresponding authors at: Department of Materials Science and Engineering, College of Engineering, Peking University, Beijing 100871, China (Y. Zheng).
E-mail addresses: yfzheng@pku.edu.cn (Y. Zheng), szYangjianan@126.com (J.-A. Yang).

https://doi.org/10.1016/j.actbio.2019.08.004
1742-7061/

clinical studies [13,14]. In most cases, MAS degrades too rapidly to maintain mechanical integrity long enough to fulfill its purpose [15]. Therefore, to overcome this hurdle, the challenge comes down to regulating the corrosion rate of the Mg alloys such that both the degradation rate and the loss of mechanical support can be tailored to the physiological needs. The complex in vivo environment is characterized by the dynamic chemical and physiological processes, mechanical and thermal loadings, and bioelectric potentials, all of which have a significant impact on the corrosion of the biodegradable devices [16,17] and are yet to be fully understood.

The chemical kinetics of the corrosion mechanism and how that interacts with the mechanical stress are the emerging topics in both theoretical and experimental studies [18,19]. As load-bearing devices function in the coronary arteries, stents are subject to cyclic loadings imposed by the arterial impulses, which leads to concerns of premature failures caused by fatigue [20-25]. It was reported that fatigue-related failures are the cause of the most part of the mechanical failures of metallic implants [26]. For stents, 78% of the stent fracture cases are associated with serious stent complications [27]. Furthermore, there is believed to be a synergetic effect of the corrosion damage and the fatigue damage (corrosion fatigue) [26,28,29], adding up to the complexity of the problem. Our previous works [28,29] reported the experimental corrosion fatigue behaviors of HP-Mg and several Mg alloys including the WE43 alloy. Wittke et al. reported the fatigue properties of the creep-resistant Mg alloy in corrosive environments [30]. Nan et al. studied the corrosion fatigue behavior of the AZ31 alloy in sodium chloride solution using the experimental method [31]. However, as pointed out by Antunes et al. [26], research of corrosion fatigue on Mg and its alloys is still scarce. It is to be noted that among the limited number of corrosion fatigue studies, nearly all of them were based on the experimental investigation of Mg and its alloys [28–31].

Numerical simulation has been proven an effective tool in understanding the underlying mechanism of corrosion as well as bridging the gap between experimental studies and clinical applications. Corrosion fatigue models have been developed for other metallic alloys [32–38], polymers [37,39], and composites [37,39-45] Generally, there are two types of approach to physically simulate the corrosion fatigue phenomenon. One approach is to look closely at the boundary where the corrosion occurs [33,34] or the fatigue crack propagates [35,36]. Several numerical methods including moving boundary and adaptive re-meshing have been adopted [5,46–48]. This moving boundary approach, while capable of accurately modeling the local events, requires a more in-depth characterization of the microscopic mechanisms. The galvanic corrosion mechanism of couples has been studied by Deshpande with a numerical model that tracks the moving boundary of the corroding materials [49]. Liu and Schlesinger proposed a mathematic model that describes microgalvanic corrosion for Mg and its alloys [50]. A numerical model for microgalvanic activity within binary phase metal alloys was developed by Deshpande using the Arbitrary-Lagrangian-Eulerian moving mesh method [51]. The importance of three-dimensional effects in fatigue design was discussed by Pook [52]. However, it is difficult to apply these models to an actual medical device, as the focus on the micro-level mechanism makes the comparison with experiments not straightforward and significantly increases the computational costs [53]. Another approach based on the continuum damage mechanics (CDM) analyzes damage processes in materials from a continuum mechanics viewpoint [32,37–45,54]. CDM can be easily implemented in the finite element (FE) framework. Hence, the CDM approach is more suitable in modeling the complex 3D geometries and loading conditions of the biodegradable stents.

For Mg alloys, Gastaldi et al. developed a continuum damage-based corrosion model under the FE framework to analyze the corrosion of coronary stents, in which they incorporated the corrosion process into the evolution function of the damage field (D) [53]. Following their work, several studies using the same approach were published, specifically focusing on uniform corrosion, pitting, stress corrosion, or strain-mediated corrosion [6,16,53,55,56]. The CDM-based phenomenological approach has been proven valid in predicting the corrosion of biodegradable metals. However, these existing FE studies do not consider the synergetic effect of corrosion and fatigue.

In this paper, we further extended the CDM-based corrosion model to account for the corrosion fatigue behaviors of Mg and its alloys. The synergistic effect of corrosion damage and fatigue damage was incorporated in the multiplicative way to specify how each mechanism contributes to the overall damage. The developed corrosion fatigue model was then implemented using the commercial FE code and a user-developed subroutine. It is often challenging to obtain the required model parameters experimentally. The advantage of having in-house experimental data of HP-Mg and WE43 alloy from our previous work was to calibrate the model by fitting parameters. Finally, the corrosion fatigue model was applied to simulate a coronary stent fabricated from HP-Mg or WE43 alloy. To the best of our knowledge, this is the first paper that numerically simulated the corrosion fatigue behavior of the MASs under cyclic loading in the physiological environment.

2. Methods

2.1. Fatigue damage model

In the CDM-based corrosion model for Mg alloys that Gastaldi et al. first developed [53], the continuum damage theory was adopted to simply focus on the macroscopic mechanical response, including stiffness and yield stress, to the presence of geometrical discontinuities or defects. The physical details of the defects are ignored. Hence, explicit modeling of the microstructure and interaction is not needed. The centerpiece of the CDM approach is an internal variable called damage field (D), which is defined as a continuous function of spatial coordinates and time. Under isotropic assumption, D is a scalar field related to the properties of materials. In particular, $D = 0$ indicates the material is undamaged, while $D = 1$ indicates the material is completely damaged and cannot sustain loads. With parameter D, an effective stress tensor σ_{ij} is defined by

$$\widetilde{\sigma}_{ij} = \frac{\sigma_{ij}}{1 - D} \tag{1}$$

where σ_{ij} is the Cauchy stress tensor. Therefore, the constitutive relation of the damaged material can be written as

$$\sigma_{ij} = \widetilde{\sigma}_{ij}(1 - D) = C_{ijkl}(1 - D)\varepsilon_{kl} \tag{2}$$

where C_{ijkl} is the fourth-order stiffness tensor of material properties.

In the corrosion model, D is used to describe the damage caused by the corrosion process. In this model, the damage field is composed of two parts: corrosion damage (D_c) and fatigue damage (D_f). For corrosion damage, the pitting model developed by Grogan et al. [6] is adopted. The damage evolution law is given by

$$\frac{dD_c}{dt} = \frac{\delta_U}{L_e}\lambda_e K_U \tag{3}$$

where t represents time and D_c is the corrosion damage field. δ_U is a characteristic dimension of the uniform corrosion process, namely, the critical thickness of the corrosion film. K_U is a parameter related to the kinetics of the uniform corrosion process. L_e is the

characteristic FE length. λ_e is an element-specific dimensionless pitting parameter. Each element on the initial exposed surface is assigned with a unique random number for the λ_e value through a standard random number generator based on Weibull distribution.

For fatigue damage, a modified damage evolution model [32] is introduced as

$$\frac{dD_f}{dN} = \frac{\sigma_e^{2q}}{B(1-D_f)^{2q}} \tag{4}$$

where N represents the number of fatigue load cycles, and D_f is the fatigue damage field. σ_e is the maximum equivalent stress of loading (i.e., Mises stress). Parameter q is a material constant that is determined by calibration. Parameter B is not only related to material but also supposed to be treated as a function of the cyclic loading.

N and t are correlated through loading frequency f:

$$N = f \cdot t \tag{5}$$

The overall damage evolution is contributed by the material damage accumulated from different degradation mechanisms, i.e., corrosion and fatigue. To combine these two damage fields, a multiplication rule is used [40]:

$$D = 1 - (1 - D_c)(1 - D_f) \tag{6}$$

The corrosion fatigue model is then implemented within a FE framework using the Abaqus/Explicit solver and user-defined subroutine (VUSDFLD) through the numerical algorithm as shown in Fig. 1. First, parameters are specified, and arrays are created. Then Abaqus/Explicit FE solver computes the stress and deformation. The stress/strain results are passed along to the user-defined subroutine VUSDFLD. For each exterior element on the surface, the damage is calculated through Eqs. (3–6). However, Eqs. (3–4) are used in a discrete form to update the damage field at time increment Δt:

$$D_c = D_{c-1} + \frac{\delta_U}{L_e}\lambda_e K_U \alpha \Delta t \tag{7}$$

$$D_f = D_{f-1} + \frac{\sigma_e^{2q}}{B(1-D_{f-1})^{2q}} f \alpha \Delta t \tag{8}$$

where D_{c-1} and D_{f-1} are the values of D_c and D_f at the previous time step, respectively. Δt is the time increment for calculation. α is the time amplification factor introduced because fatigue computation is usually time-consuming. It saves time in calculation by multiplying the time step by the factor α. In this way, a longer time can be simulated with the same step numbers. Results from Eqs. (7) and (8) are substituted into Eq. (6) to obtain the overall damage D. These steps are repeated for every time increment step. When the material's damage accumulates and the damage D reaches to 1, the corresponding element is then removed from the FE mesh and the corrosion surface is updated.

2.2. Experimental results and model calibration

The corrosion fatigue model is calibrated with the experimental results of our previous studies [28,29]. The corrosion fatigue properties (corrosion rate under cyclic loading) of HP-Mg and WE43 alloy are separately tested in these two studies. The corrosion rate used in this study is defined as the mass loss per area during a specific period. According to ASTM-E466-96 [57], fatigue specimens with a circular cross-section, 5 mm diameter and 10 mm gauge length are used for the corrosion fatigue test to calibrate the parameters of the numerical model. The values of parameters

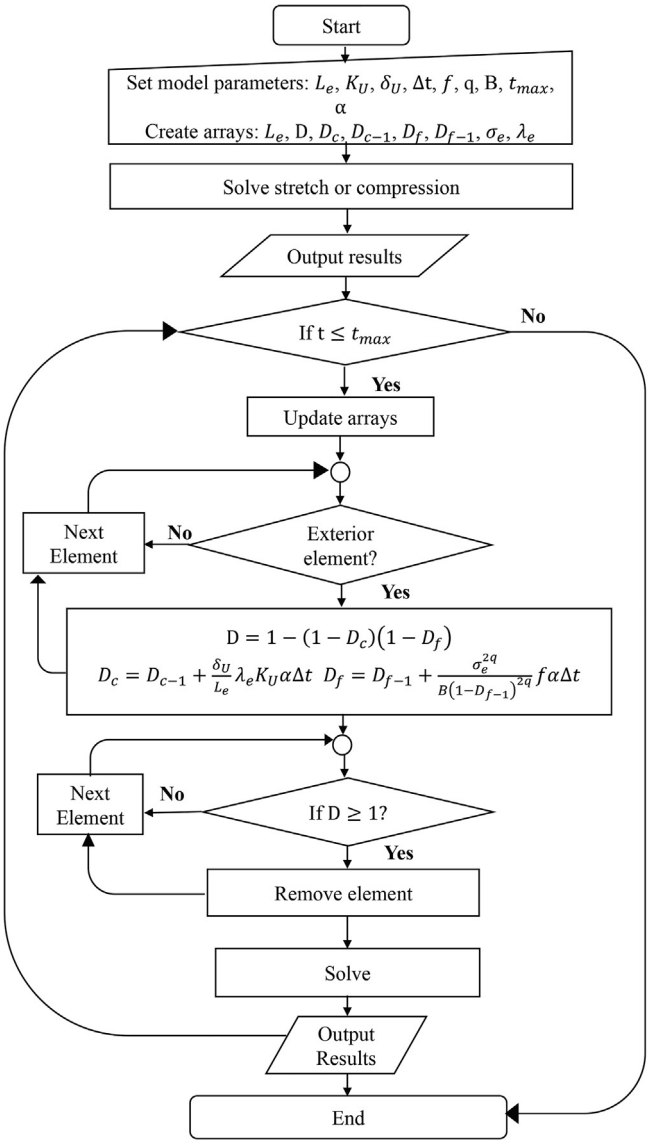

Fig. 1. Flowchart of the corrosion fatigue algorithm.

B and q are adjusted until the resulting corrosion rate from the model can fit the experimental results within an error less than 1%. A standard test specimen is shown in Fig. 2(a), wherein the red part represents the test region. Fig. 2(b) shows the FE model in Abaqus simulation to replicate the test specimen. Considering that both ends of the sample are designed for clamping during the experimental testing, only the test region is simulated and the two ends of the test region are not treated as external surfaces exposed to environment. All the boundaries are set to free, and axial pressure is applied to both ends of the sample for uniaxial loading. The pressure is set at cyclic load to match with the experimental test setup, more specifically, in sinusoidal loading with frequency = 10 Hz and stress ratio $R = -1$.

To obtain the mechanical parameters of the material, the uniaxial tensile test is also simulated with Abaqus/Standard. The dimensions of the model are the same as those of the fatigue sample. A quasi-static axial loading is simulated by applying a displacement boundary condition to both ends of the sample. Other boundaries are regarded as the free boundaries. All the calibrations are accomplished by the best fit of the experimental data.

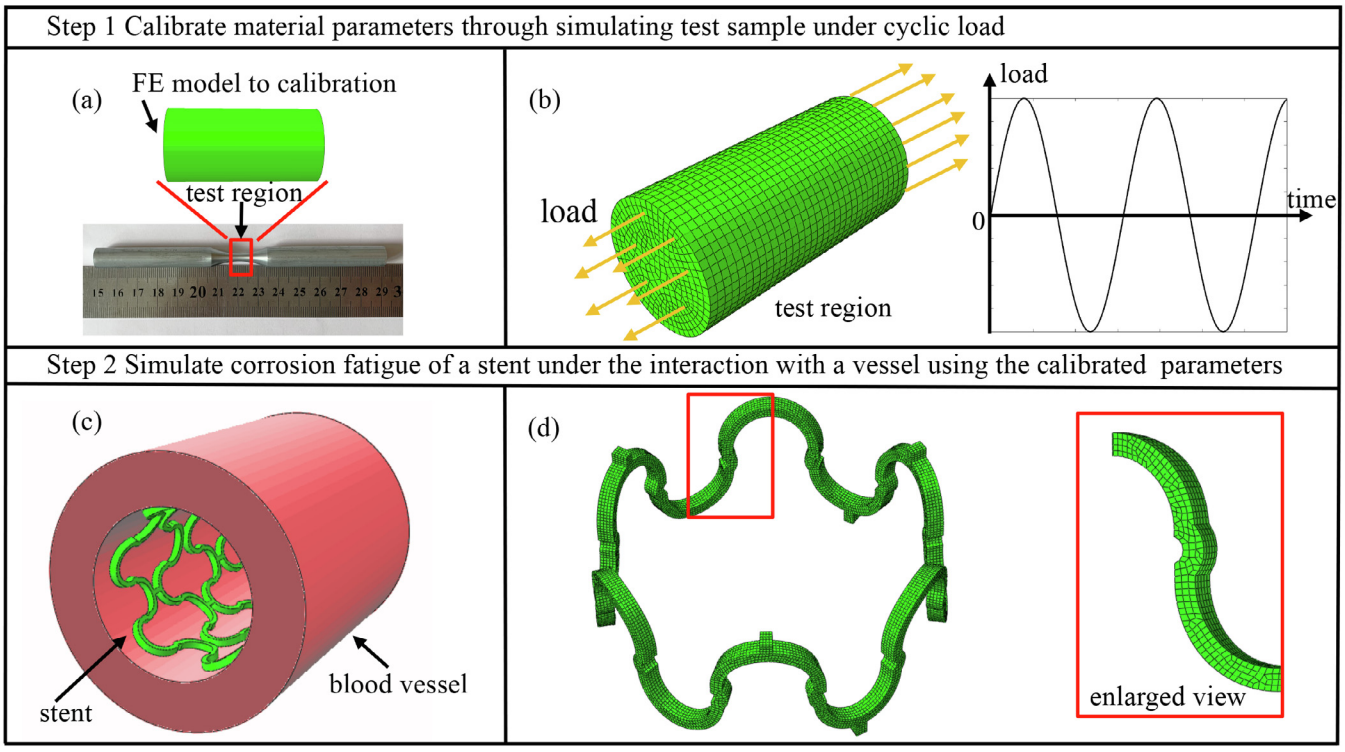

Fig. 2. (a) Sample used for experimental test, in which the red part represents the test region. (b) FE model of the test region in (a). (c) FE model of the stent and the artery. (d) A ring structure of the stent with an enlarged view of the stent strut. (For interpretation of the references to color in this figure legend, the reader is referred to the web version of this article.)

2.3. Stent application

A stent model is established with the geometry demonstrated in Fig. 2(d). As shown in the figure, the whole stent is a repeating sinusoidal ring pattern with six complete sinusoidal periods in the circular direction and four rings in the axis direction. Fig. 2 (d) shows only 1 ring of the stent model, which has a diameter of 3.2 mm. With four rings in the axis direction, the length of the stent is 5.36 mm. The stent strut is shown in the enlarged view in Fig. 2(d), which has a width of 108 μm and a thickness of 150 μm.

The artery is modeled as a straight tube. The blood vessel consists of three layers, namely, intima, media, and adventitia, the thicknesses of which can be found in Ref. [58]. Each layer was modeled as an isotropic hyperelastic material using a six-order polynomial strain energy density function according to Gervaso et al. [59]. The density of the tissue was set to 1.12 g/cm^3 according to Gastaldi et al. [53]. The mechanical anisotropy of the arterial tissue, which was assessed by Holzapfel et al. [58]; the prestretch of the vessel; and the stenosis should be taken into account to determine the mechanical property of the artery. However, the scope of this work is focused on the corrosion fatigue modeling of the intravascular stent instead of the artery itself. For simplicity, the artery is modeled only to translate the impulse load to the stent by surface contact.

In stent application, the vascular is modeled as an annular wall, with 5.12 mm OD, 3.2 mm ID, and 6 mm length. The vascular is assembled around the stent as shown in Fig. 2(c). The length is selected to have extra coverage of the blood vessel over the stent at both ends. The inner surface of the artery and the outer surface of the stent contact each other with the general contact algorithm in the Abaqus package to simulate the stent–artery interaction. This general contact algorithm allows for the automatic redefinition of contact surfaces by the Abaqus solver following element removal [60] and the continued modeling of the stent–artery interaction as the material corrodes. For the tangential contract, the coefficient of friction is assumed to be 0.2 [6]. The normal contact was set as the default "hard" contact. The stent and the artery were both meshed with the C3D8R element type in Abaqus, an 8-node linear brick element with reduced integration [61]. The average characteristic length of the mesh is 0.02 mm, following a mesh convergence study in corrosion simulations through appropriate scaling of the corrosion model parameters [6]. The stent was meshed with 130,000 C3D8R elements, and the artery was meshed with 60,000 C3D8R elements.

The pulsatile loading was applied to the stent at 72 heartbeats per minute according to the US FDA recommendation [62]. The vessel pulses radially in a sinusoidal form with an amplitude of 0.04 mm [63]. In this paper, the vessel was simulated with the average values of a human.

2.4. Statistical analysis

Statistical analysis was performed with OriginPro 9.0 software package (OriginLab Inc. Northampton. USA). Statistical significance of difference between groups was assessed by one-way analysis of variance (ANOVA) followed by post hoc Tukey's multiple comparison test. P values less than 0.05 were considered statistically significant. All fitting results had an error less than 1%.

3. Results

3.1. Calibration results

3.1.1. Calibration of mechanical properties

The experimental results of HP-Mg and WE43 alloy from our previous studies [28,29] are used for the calibration of mechanical

properties in the corrosion fatigue model. Fig. 3(a) and 3(b) depict the respective stress–strain curves of HP-Mg and WE43 alloy.

The solid lines shown in Fig. 3(a) and 3(b) are plotted from the actual experimental data. The input of the mechanical parameters in the numerical models is determined by the best fit of undamaged materials, shown as black dotted lines. These parameters are listed in Table 1. The reduction in the mechanical integrity of the material induced by corrosion fatigue can be characterized by modifying the material mechanical parameters with different values of *D*. Four exemplary situations are simulated representing the material properties of elements, with *D* values ranging from 0 to 1, in increments of 0.25. Based on the assumption that reduction in the load-bearing capacity of the element is directly related to the damage field, the stress–strain curves are produced by scaling down the Young's modulus of the undamaged materials by *D*. It is shown that the stress decreases as the damage field *D* increases at the same strain level as shown in Fig. 3(a) and 3(b), which is consistent with the experimental observation of the loss of mechanical integrity [6,16].

3.1.2. Damage evolution calibration

In Fig. 3(c) and 3(d), the respective corrosion rates of HP-Mg and WE43 alloy are used to calibrate the parameters in the damage evolution Eqs. (7) and (8). These corrosion rates are for a standard test sample immersed in a simulated body fluid (SBF) subject to fatigue loading. Experimental data from our previous studies [28,29] are displayed as bars in the figures. Model results under the same cyclic loading are displayed as data point markers in these two plots. Parameters that resulted from this calibration are listed in Table 2. As shown in Fig. 3(c) and 3(d), the magnitude of cyclic loading has a significant influence on corrosion rate in the SBF. Consequently, the fatigue loading can lead to corrosion acceleration in a way that the material could lose its load-bearing capacity even before the expected time point. When the cyclic loading reaches a threshold value, the corrosion rate rapidly elevates when compared with that in the reference sample that has no fatigue loading applied. This threshold value is different for HP-Mg and WE43 alloy. From limited data points, the threshold value for HP-Mg should be less than 50 MPa, while that for WE43 alloy should be somewhere between 110 MPa and 120 MPa. More experimental tests are required to better demonstrate the trends.

Fig. 4 shows the contour plots of the damage fields of both samples. The HP-Mg sample is subjected to 70 MPa cyclic load, and for the WE43 alloy sample, the cyclic load is 120 MPa. At approximately 250 h of simulation, the HP-Mg sample has damage values of nearly all elements reaching 1, and some elements have already been deleted from the model, indicative of a fully damaged material. For the WE43 alloy, the material is fully damaged at approximately 35 h, much faster than that for HP-Mg. The damage fields of HP-Mg and WE43 alloy at half time to the fully damaged state are also shown in Fig. 4. The corrosion damage and fatigue damage are displayed separately to compare their differences. It can be seen that the fatigue damage is much larger than the corrosion damage for both HP-Mg and WE43 alloy. Here, the fatigue damage dominates when the cyclic loading is applied at a frequency of 10 Hz. Another observation is the inhomogeneous distribution of the damage field, showing a pitting type of degradation.

3.2. Modeling the corrosion fatigue of Mg alloy stent

The application of Mg alloy in stents is simulated using the calibrated corrosion fatigue model for both the HP-Mg and the WE43 alloy. The damage fields at 28 h of simulation are displayed in Fig. 5. In addition to the total damage, the corrosion damage and the fatigue damage are decoupled and displayed here as well. The scale of the color legend was chosen to be different, as the corrosion fatigue damage differs between HP-Mg and WE43 alloy. It is found that the WE43 stent degrades more rapidly than the HP-Mg stent, which has been seen in the sample tests in section 3.1.2. It is

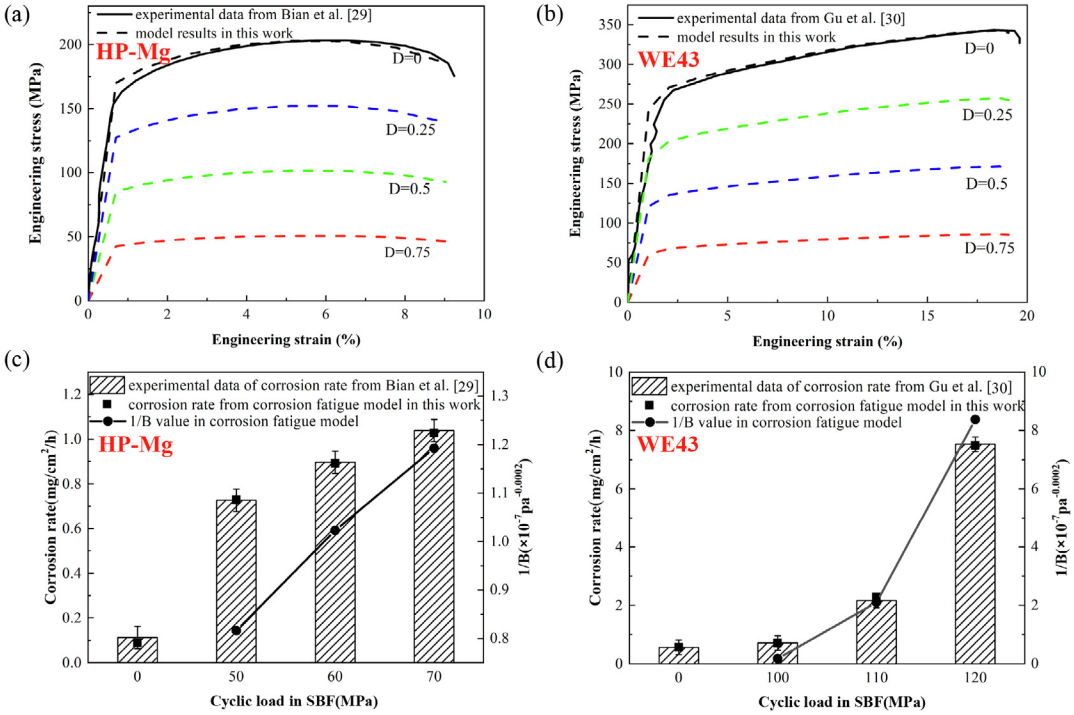

Fig. 3. Stress–strain curve of (a) HP-Mg and (b) WE43 alloy; solid lines represent experimental data, and dashed lines represent results from this model. Sample corrosion rate of (c) HP-Mg and (d) WE43 alloy; bars represent experimental data, and lines represent results from this model. Correlation of parameter B with cycle load for (c) HP-Mg and (d) WE43 alloy.

Table 1
Parameters of mechanical property of HP-Mg and WE43 alloy.

HP-Mg			WE43 alloy		
Young's modulus (MPa)	Poisson's ratio	Density (kg/m^3)	Young's modulus (MPa)	Poisson's ratio	Density (kg/m^3)
83,600	0.3	1738	23,300	0.3	1830
Yield stress (MPa)	Plastic strain (%)		Yield stress (MPa)		Plastic strain (%)
153.561	0		255.04		0
163.248	0.211		267.192		0.455
179.915	1.044		285.962		2.662
186.752	1.603		295.899		4.351
196.724	2.911		303.628		5.844
202.137	4.367		313.565		7.792
203.276	5.116		322.397		9.545
203.276	5.876		336.751		13.961
201.994	6.646		343.375		16.494
199.003	7.373		342.271		17.532
185.613	8.449		333.438		17.792

Table 2
Parameters of corrosion fatigue property of HP-Mg and WE43 alloy.

HP-Mg				WE43			
q	$\delta_U K_U(mm/s)$		α	q	$\delta_U K_U(mm/s)$		α
0.0001	3.241×10^{-8}		10^6	0.0001	1.942×10^{-7}		10^5
Cyclic load	50 MPa	60 MPa	70 MPa	Cyclic load	100 MPa	110 MPa	120 MPa
B (MPa)	12.254	9.7732	8.3859	B (MPa)	56.216	4.7739	1.1935

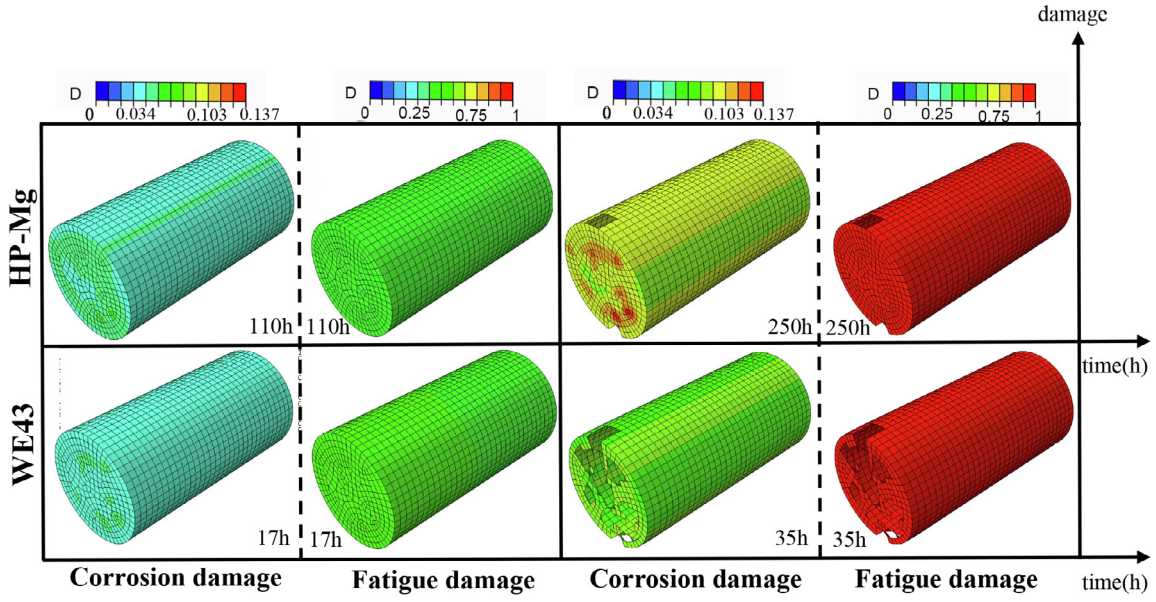

Fig. 4. Contour plots of the damage field of the test samples for HP-Mg and WE43 alloy.

worth mentioning that the overall degradation of the stent is dominated by corrosion damage for both the materials, contrasting to that shown in the sample tests.

4. Discussion

4.1. Parameter determination

Most parameters in this model can be easily determined by the method mentioned above except for the value of B in Eqs. (3) and (7). There is no such value of B that can be suitable for all the loading cases just as mentioned above.

Fig. 3(c) and 3(d) show the relationship between B and cyclic load of HP-Mg and WE43 alloy, respectively. A linear fitting is used for HP-Mg assuming the proportional relationship of 1/B and the load:

$$\frac{1}{B} = 1.882 \times 10^{-9}\sigma_e - 1.188 \times 10^{-8} \tag{9}$$

A piecewise linear fitting is applied for the WE43 alloy:

$$\frac{1}{B} = \begin{cases} 1.917 \times 10^{-8}\sigma_e - 1.899 \times 10^{-6} (\sigma_e \le 110MPa) \\ 6.284 \times 10^{-8}\sigma_e - 6.703 \times 10^{-6} (\sigma_e > 110MPa) \end{cases} \tag{10}$$

First, we investigated the stress distribution in the stent at maximum deformation. Fig. 6 exhibits stress distribution in the stent at maximum deformation. It can be found that the distribution profile is nearly the same for these two kinds of material. This result is reasonable because these two cases are nearly the same except

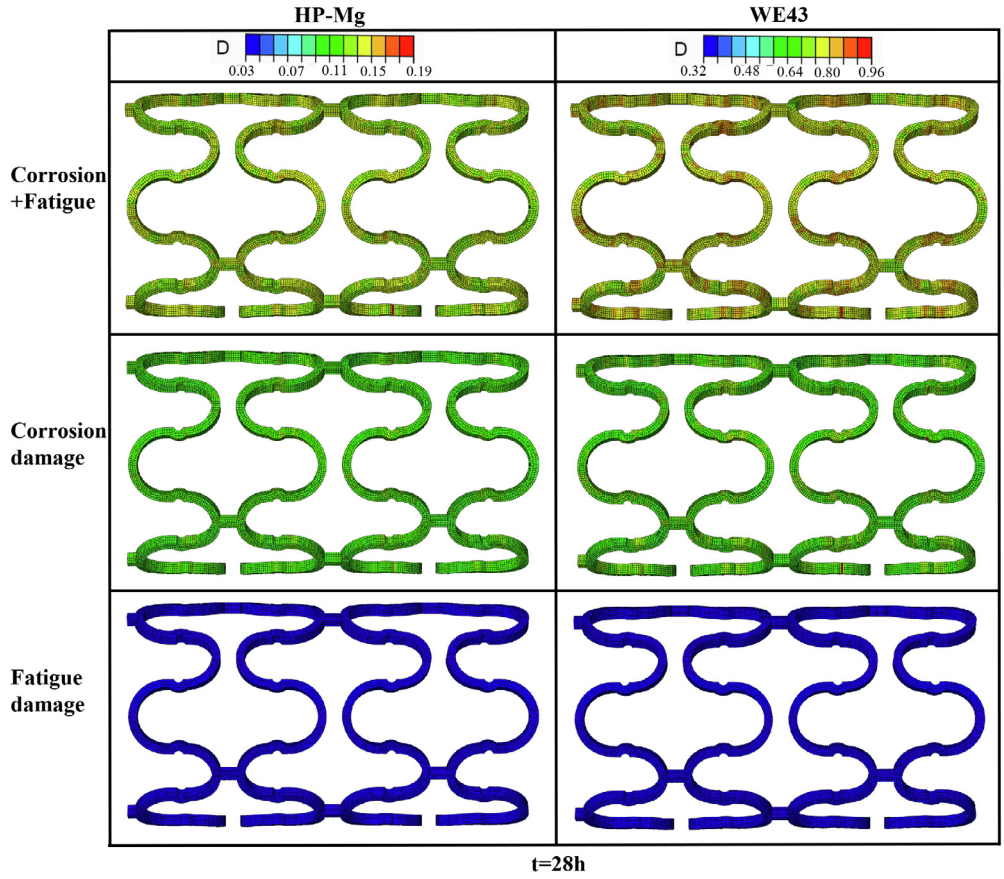

Fig. 5. Contour plots of the damage field of the stents for HP-Mg and WE43 alloy.

for materials that can only influent stress magnitude while having no effects on the distribution profile. Additionally, the average stress values are calculated through the distributions. Finally, the average values, which are 120 MPa and 150 MPa, are used to obtain B values according to Eqs. (8) and (9) for HP-Mg and WE43 alloy, respectively.

4.2. Fatigue damage and degradation rate

The total mass loss for the stent is contributed by both the corrosion damage and the fatigue damage. The results have been shown in Fig. 5 in terms of how the damage fields were distributed spatially over the entire model. Fig. 7 depicts the mass loss due to damage with time for the stents of both HP-Mg and WE43 alloy. The total mass loss is dominated by pitting damage for HP-Mg in Fig. 7 (a) and similarly for the WE43 alloy in Fig. 7(b). This is contrary to the observation in the in vitro sample tests. The reason stent results are different from sample results may be attributed to the environment difference between in vivo and in vitro. The most important factor is the load frequency. It is evident that load frequency markedly affects the damage evolution according to Eq. (8). The cyclic loading for in vivo stent application was applied at 72 beats per minute (1.2 Hz), while for the vitro sample tests, the cyclic loading was at a much higher frequency (10 Hz). Although the fatigue damage does not dominate for a stent implanted in vivo, the mass loss due to fatigue damage still takes

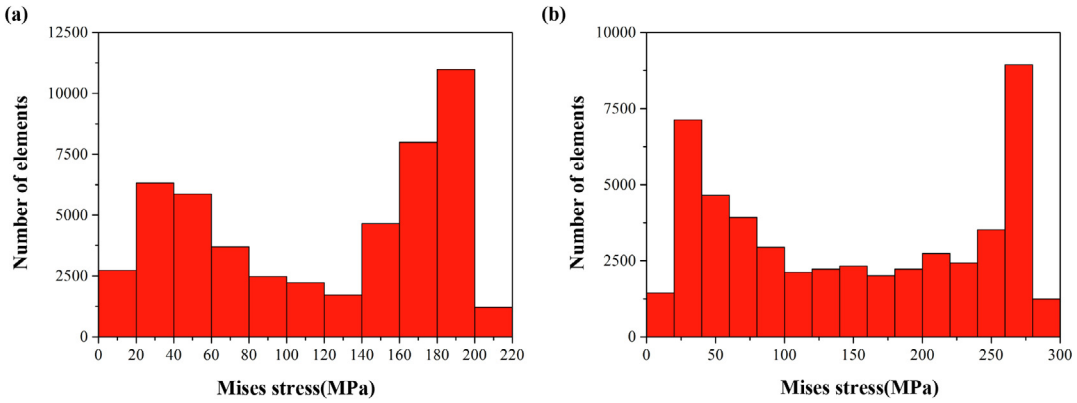

Fig. 6. Stress distribution statistical bar chart for (a) HP-Mg and (b) WE43 alloy.

up approximately 20% of the total mass loss for HP-Mg as shown in Fig. 7(a). The fatigue damage is more pronounced in the stent of the WE43 alloy as shown in Fig. 7(b), where the fatigue damage contributed to nearly half of the total mass loss. The simulation results clearly showed that, when studying the in vivo degradation of MASs, the fatigue effect should always be factored in. The acceleration in degradation by fatigue loading could potentially lead to the premature failure of stents. This conclusion is drawn in accordance with the report by Antunes et al. [26]. By comparing the time to degradation, it can be seen that the HP-Mg stent completely degraded at approximately 275 h, while the WE43 alloy stent completely degraded at approximately 45 h. Here the fatigue corrosion model demonstrated that the WE43 stent degrades approximately 6 times faster than the HP-Mg stent. The degradation rate is one of the key characteristics to be considered in developing coronary stents. The corrosion fatigue model in this work could provide a better insight into the degradation behavior by predicting the overall degradation rate.

4.3. Mechanical integrity and critical location

The purpose of a biodegradable Mg stent is first to provide the required mechanical support and then to degrade. In this section, we discuss the loss of mechanical integrity due to the evolving damage and the critical location of the damage. A stent mainly supports the blood vessel to prevent it from elastic arterial recoil. Therefore, radial support is a significant mechanical property used to evaluate stent performance. To assess the radial support, a compression test is performed with the FE method using the calibrated corrosion fatigue model. All the details are the same except that the load is applied as compression only instead of a cyclic load. The critical location where the maximum stress occurs has the highest probability of failure, susceptible to the loss of support capability in the stent. Hence, maximum stress has been regarded as an index for evaluating the mechanical support capacity. Fig. 8(a) illustrates the development of maximum stress with the progression of compression. It is shown that the maximum stresses decrease with the damage increasing regardless of the materials, which implies that evolving damage causes the loss of mechanical support capacity in the stent. As shown in Fig. 8(a), both the HP-Mg and WE43 stents have yielded and entered into the plastic region in the compression test, which is in line with the results reported by Galvin et al. [16].

Radial stiffness is not directly calculated from the model. Instead, the radial force at a certain degree of radial compression is plotted to characterize the radial stiffness, as shown in Fig. 8 (b). The radial stiffness reduces linearly with the evolvement of damage for both HP-Mg and WE43 alloy stents. The radial forces of them are nearly the same. The inserted picture in Fig. 8(b) shows the removal of elements in a WE43 alloy strut as the damage of the whole stent reaches 75%, indicating the critical location of the damage. The ability to identify the critical location provides the theoretical basis for design optimization.

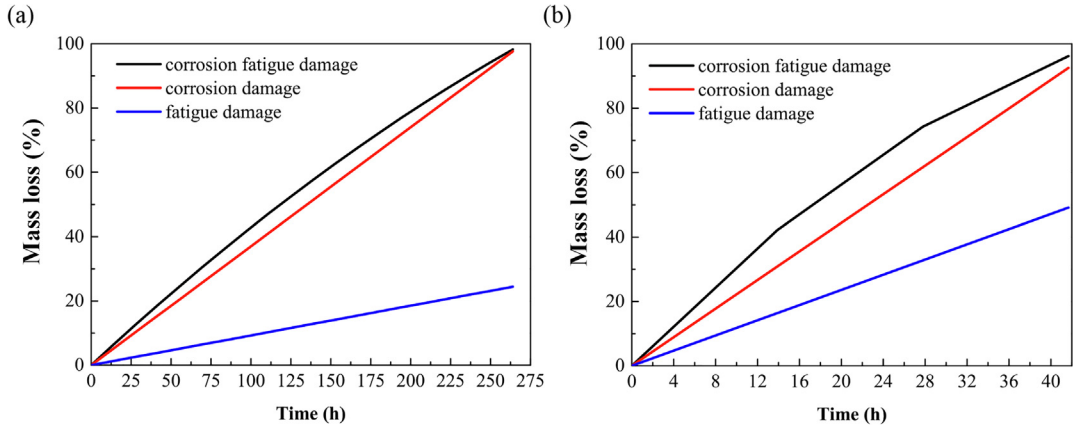

Fig. 7. Mass loss due to corrosion and fatigue damage for (a) HP-Mg and (b) WE43 alloy.

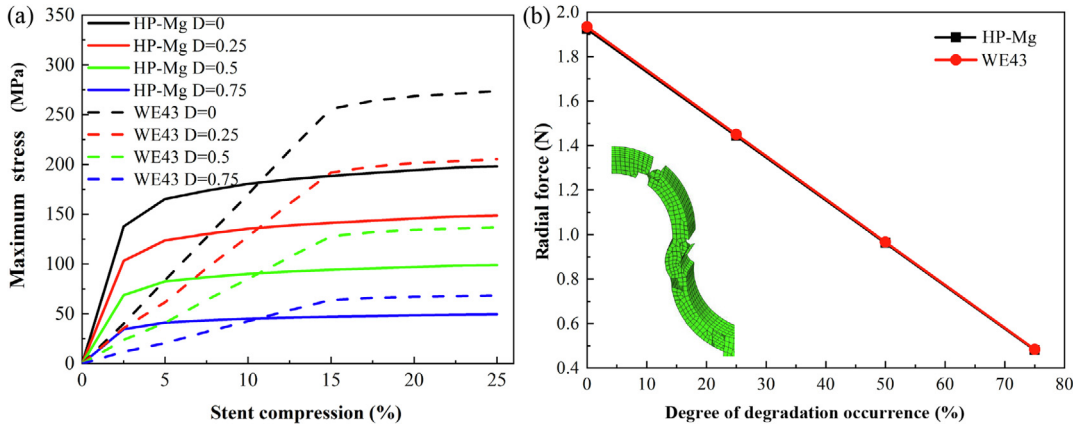

Fig. 8. (a) Maximum stress in the stent varies with stent compression. Solid lines represent HP-Mg and dashed lines represent the WE43 alloy. (b) Radial force declines with corrosion development. The inserted picture shows the element delegation of a strut.

4.4. Model applications

Although this study discussed only the application of the corrosion fatigue model in MASs, our model can be easily extended to other biodegradable alloy systems such as Fe and Zn. In the meso-scale model, the evolution formula of fatigue damage for other metals can be derived by assuming a brittle damage mechanism, which has been discussed in the work by Amiri et al. [34]. Similarly, the model parameters are fitted with the experimental observations. This paper presented a generic numerical framework in assessing the corrosion fatigue property of biodegradable metals. The validation of the numerical model is based on the in vitro test of the samples under cyclic load in the corrosion environment. Then, the calibrated model can be applied to study the corrosion fatigue properties of actual medical devices, with much more complex geometry and load conditions.

5. Conclusions

In this study, a numerical FE model was established to simulate the corrosion fatigue behavior of the biodegradable Mg alloys. The mechanical and damage parameters were calibrated by the in vitro sample tests of HP-Mg and WE43 alloy. As an application, the corrosion fatigue model was used to simulate the in vivo deformation of the coronary stents fabricated using HP-Mg or WE43 alloy. The trends in the degradation rate, loss of mechanical radial support, and the critical location of degradation and deformation were evaluated from the simulation results. The analysis has proven that these simulation results are in good accordance with the experimental results or other research work. It is found that fatigue loads or cyclic stresses have an important effect on the acceleration of the degradation rate and loss of mechanical integrity. Therefore, the corrosion fatigue model can be used as a numerical tool to help understand the biodegradable process of MASs and improve fatigue durability.

Acknowledgments

This work was supported by the National Natural Science Foundation of China (Grant No. 51431002 and 51871004) and NSFC/RGC Joint Research Scheme (Grant No. 51661165014).

References

[1] Y.F. Zheng, X.N. Gu, F. Witte, Biodegradable metals, Mater. Sci. Eng. R Rep. 77 (2014) 1–34.
[2] R. Erbel, C. Di Mario, J. Bartunek, J. Bonnier, B. de Bruyne, F.R. Eberli, P. Erne, M. Haude, B. Heublein, M. Horrigan, C. Ilsley, D. Böse, J. Koolen, T.F. Lüscher, N. Weissman, R. Waksman, Temporary scaffolding of coronary arteries with bioabsorbable magnesium stents: a prospective, non-randomised multicentre trial, Lancet 369 (9576) (2007) 1869–1875.
[3] M.P. Staiger, A.M. Pietak, J. Huadmai, G. Dias, Magnesium and its alloys as orthopedic biomaterials: A review, Biomaterials 27 (9) (2006) 1728–1734.
[4] H. Hermawan, D. Dube, D. Mantovani, Developments in metallic biodegradable stents, Acta Biomater. 6 (5) (2010) 1693–1697.
[5] J.A. Grogan, S.B. Leen, P.E. McHugh, Optimizing the design of a bioabsorbable metal stent using computer simulation methods, Biomaterials 34 (33) (2013) 8049–8060.
[6] J.A. Grogan, B.J. O'Brien, S.B. Leen, P.E. McHugh, A corrosion model for bioabsorbable metallic stents, Acta Biomater. 7 (9) (2011) 3523–3533.
[7] J.A. Grogan, S.B. Leen, P.E. McHugh, Comparing coronary stent material performance on a common geometric platform through simulated bench testing, J. Mech. Behav. Biomed. Mater. 12 (2012) 129–138.
[8] M. Haude, R. Erbel, P. Erne, S. Verheye, H. Degen, D. Böse, P. Vermeersch, I. Wijnbergen, N. Weissman, F. Prati, R. Waksman, J. Koolen, Safety and performance of the drug-eluting absorbable metal scaffold (DREAMS) in patients with de-novo coronary lesions: 12 month results of the prospective, multicentre, first-in-man BIOSOLVE-I trial, Lancet 381 (9869) (2013) 836–844.
[9] P.W. Serruys, P. de Jaegere, F. Kiemeneij, C. Macaya, W. Rutsch, G. Heyndrickx, H. Emanuelsson, J. Marco, V. Legrand, P. Materne, J. Belardi, U. Sigwart, A. Colombo, J.J. Goy, P. van den Heuvel, J. Delcan, M.-A. Morel, A Comparison of Balloon-Expandable-Stent Implantation with Balloon Angioplasty in Patients with Coronary Artery Disease, N. Engl. J. Med. 331 (8) (1994) 489–495.
[10] B. Heublein, R. Rohde, V. Kaese, M. Niemeyer, W. Hartung, A. Haverich, Biocorrosion of magnesium alloys: a new principle in cardiovascular implant technology?, Heart 89 (6) (2003) 651–656
[11] R. Waksman, R. Pakala, P.K. Kuchulakanti, R. Baffour, D. Hellinga, R. Seabron, F. O. Tio, E. Wittchow, S. Hartwig, C. Harder, Safety and efficacy of bioabsorbable magnesium alloy stents in porcine coronary arteries, Catheter Cardio. Int. 68 (4) (2006) 607–617.
[12] C. Di Mario, H. Griffiths, O. Goktekin, N. Peeters, J. Verbist, M. Bosiers, K. Deloose, B. Heublein, R. Rohde, V. Kasese, Drug-eluting bioabsorbable magnesium stent, J. Int. Cardiol. 17 (6) (2004) 391–395.
[13] J.S. Forrester, M. Fishbein, R. Helfant, J. Fagin, A paradigm for restenosis based on cell biology: clues for the development of new preventive therapies, J. Am. Coll. Cardiol. 17 (3) (1991) 758–769.
[14] P. Serruys, H. Luijten, K. Beatt, R. Geuskens, P. De Feyter, M. van den Brand, J. Reiber, H. Ten Katen, G.A. van Es, P. Hugenholtz, Incidence of restenosis after successful coronary angioplasty: a time-related phenomenon. A quantitative angiographic study in 342 consecutive patients at 1, 2, 3, and 4 months, Circulation 77 (2) (1988) 361–371.
[15] A. Drynda, T. Hassel, R. Hoehn, A. Perz, F.-W. Bach, M. Peuster, Development and biocompatibility of a novel corrodible fluoride-coated magnesium-calcium alloy with improved degradation kinetics and adequate mechanical properties for cardiovascular applications, J. Biomed. Mater. Res. Part A 9999A (2009).
[16] E. Galvin, D. O'Brien, C. Cummins, B.J. Mac Donald, C. Lally, A strain-mediated corrosion model for bioabsorbable metallic stents, Acta Biomater. 55 (2017) 505–517.
[17] R. Baboian, Corrosion tests and standards: application and interpretation, 1995.
[18] G. Song, A. Atrens, Understanding Magnesium Corrosion—A Framework for Improved Alloy Performance, Adv. Eng. Mater. 5 (12) (2003) 837–858.
[19] Z. Shen, M. Zhao, D. Bian, D. Shen, X. Zhou, J. Liu, Y. Liu, H. Guo, Y. Zheng, Predicting the degradation behavior of magnesium alloys with a diffusion-based theoretical model and in vitro corrosion testing, J. Mater. Sci. Technol. 35 (7) (2019) 1393–1402.
[20] M. Niinomi, Fatigue characteristics of metallic biomaterials, Int. J. Fatigue 29 (6) (2007) 992–1000.
[21] A. Vadiraj, M. Kamaraj, Effect of surface treatments on fretting fatigue damage of biomedical titanium alloys, Tribol. Int. 40 (1) (2007) 82–88.
[22] C. Fleck, D. Eifler, Corrosion, fatigue and corrosion fatigue behaviour of metal implant materials, especially titanium alloys, Int. J. Fatigue 32 (6) (2010) 929–935.
[23] N.J. Giori, Unexpected finding of a fractured metal prosthetic femoral head in a nonmodular implant during revision total hip arthroplasty, J. Arthropl. 25 (4) (2010). 659.e13-659.e15.
[24] J. Chao, V. López, Failure analysis of a Ti6Al4V cementless HIP prosthesis, Eng. Fail. Anal. 14 (5) (2007) 822–830.
[25] X.-C. Zhou, F. Yang, X.-Y. Gong, M. Zhao, Y.-F. Zheng, Z.-L. Sun, New nitinol endovascular stent-graft system for abdominal aortic aneurysm with finite element analysis and experimental verification, Rare Met. 38 (6) (2019) 495–502.
[26] R.A. Antunes, M.C.L. de Oliveira, Corrosion fatigue of biomedical metallic alloys: mechanisms and mitigation, Acta Biomater. 8 (3) (2012) 937–962.
[27] G. Nakazawa, A.V. Finn, M. Vorpahl, E. Ladich, R. Kutys, I. Balazs, F.D. Kolodgie, R. Virmani, Incidence and predictors of drug-eluting stent fracture in human coronary artery a pathologic analysis, J. Am. Coll. Cardiol. 54 (21) (2009) 1924–1931.
[28] D. Bian, W. Zhou, Y. Liu, N. Li, Y. Zheng, Z. Sun, Fatigue behaviors of HP-Mg, Mg-Ca and Mg-Zn-Ca biodegradable metals in air and simulated body fluid, Acta Biomater. 41 (2016) 351–360.
[29] X.N. Gu, W.R. Zhou, Y.F. Zheng, Y. Cheng, S.C. Wei, S.P. Zhong, T.F. Xi, L.J. Chen, Corrosion fatigue behaviors of two biomedical Mg alloys - AZ91D and WE43 - In simulated body fluid, Acta Biomater. 6 (12) (2010) 4605–4613.
[30] P. Wittke, M. Klein, F. Walther, Corrosion fatigue behaviour of creep-resistant magnesium alloy Mg-4Al-2Ba-2Ca, Proc. Eng. 74 (2014) 78–83.
[31] Z. Nan, S. Ishihara, T. Goshima, Corrosion fatigue behavior of extruded magnesium alloy AZ31 in sodium chloride solution, Int. J. Fatigue 30 (7) (2008) 1181–1188.
[32] M. Wang, Q. Fei, P. Zhang, A modified fatigue damage model for high-cycle fatigue life prediction, Adv. Mater. Sci. Eng. 2016 (2016) 1–7.
[33] P. Hu, Q. Meng, W. Hu, F. Shen, Z. Zhan, L. Sun, A continuum damage mechanics approach coupled with an improved pit evolution model for the corrosion fatigue of aluminum alloy, Corros. Sci. 113 (2016) 78–90.
[34] M. Amiri, A. Arcari, L. Airoldi, M. Naderi, N. Iyyer, A continuum damage mechanics model for pit-to-crack transition in AA2024-T3, Corros. Sci. 98 (2015) 678–687.
[35] T. Sudarshan, T. Srivatsan, D. Harvey, Ii, Fatigue processes in metals—role of aqueous environments, Eng. Fract. Mech. 36 (6) (1990) 827–852.
[36] O. Aslan, S. Quilici, S. Forest, Numerical modeling of fatigue crack growth in single crystals based on microdamage theory, Int. J. Damage Mech. 20 (5) (2011) 681–705.
[37] Y. Liu, S. Mahadevan, A unified multiaxial fatigue damage model for isotropic and anisotropic materials, Int. J. Fatigue 29 (2) (2007) 347–359.
[38] Z.-Y. Han, X.-G. Huang, Y.-G. Cao, J.-Q. Xu, A nonlinear cumulative evolution model for corrosion fatigue damage, J. Zhejiang Univ. Sci. A 15 (6) (2014) 447–453.

[39] F. Meraghni, H. Nouri, N. Bourgeois, C. Czarnota, P. Lory, Parameters identification of fatigue damage model for short glass fiber reinforced polyamide (PA6-GF30) using digital image correlation, Proc. Eng. 10 (2011) 2110–2116.
[40] G.P. Hammi Y, Horstemeyer M F., Multiscale Concrete Modeling of Aging Degradation[R], (2015).
[41] J. Degrieck, W. Van Paepegem, Fatigue damage modeling of fibre-reinforced composite materials: Review, Appl. Mech. Rev. 54 (4) (2001).
[42] W. Van Paepegem, J. Degrieck, P. De Baets, Finite element approach for modelling fatigue damage in fibre-reinforced composite materials, Compos. B Eng. 32 (7) (2001) 575–588.
[43] Y. Hua, A.D. Crocombe, M.A. Wahab, I.A. Ashcroft, Modelling environmental degradation in EA9321-bonded joints using a progressive damage failure model, J. Adhes. 82 (2) (2006) 135–160.
[44] Y. Hua, A.D. Crocombe, M.A. Wahab, I.A. Ashcroft, Continuum damage modelling of environmental degradation in joints bonded with E32 epoxy adhesive, J. Adhes. Sci. Technol. 21 (2) (2007) 179–195.
[45] R. Desmorat, Damage and fatigue, Revue Européenne de Génie Civil 10 (6–7) (2006) 849–877.
[46] J.A. Grogan, S.B. Leen, P.E. McHugh, A physical corrosion model for bioabsorbable metal stents, Acta Biomater. 10 (5) (2014) 2313–2322.
[47] P. Bajger, J.M. Ashbourn, V. Manhas, Y. Guyot, K. Lietaert, L. Geris, Mathematical modelling of the degradation behaviour of biodegradable metals, Biomech. Model. Mechanobiol. 16 (1) (2017) 227–238.
[48] W. Sun, G. Liu, L. Wang, T. Wu, Y. Liu, An arbitrary Lagrangian-Eulerian model for studying the influences of corrosion product deposition on bimetallic corrosion, J. Solid State Electr. 17 (3) (2012) 829–840.
[49] K.B. Deshpande, Validated numerical modelling of galvanic corrosion for couples: Magnesium alloy (AE44)–mild steel and AE44–aluminium alloy (AA6063) in brine solution, Corros. Sci. 52 (10) (2010) 3514–3522.
[50] L.J. Liu, M. Schlesinger, Corrosion of magnesium and its alloys, Corros. Sci. 51 (8) (2009) 1733–1737.
[51] K.B. Deshpande, Numerical modeling of micro-galvanic corrosion, Electrochim. Acta 56 (4) (2011) 1737–1745.
[52] A. Campagnolo, F. Berto, L. Pook, Three-dimensional effects on cracked discs and plates under nominal Mode III loading, Frattura ed Integrità Strutturale 9 (34) (2015).
[53] D. Gastaldi, V. Sassi, L. Petrini, M. Vedani, S. Trasatti, F. Migliavacca, Continuum damage model for bioresorbable magnesium alloy devices – Application to coronary stents, J. Mech. Behav. Biomed. Mater. 4 (3) (2011) 352–365.
[54] D. Kondo, H. Welemane, F. Cormery, Basic concepts and models in continuum damage mechanics, Revue Européenne de Génie Civil 11 (7–8) (2007) 927–943.
[55] W. Wu, D. Gastaldi, K. Yang, L. Tan, L. Petrini, F. Migliavacca, Finite element analyses for design evaluation of biodegradable magnesium alloy stents in arterial vessels, Mater. Sci. Eng., B 176 (20) (2011) 1733–1740.
[56] L. Petrini, W. Wu, D. Gastaldi, L. Altomare, S. Farè, F. Migliavacca, A.G. Demir, B. Previtali, M. Vedani, Development of biodegradable magnesium alloy stents with coating, Frattura ed Integrità Strutturale 8 (29) (2014) 364–375.
[57] A. Standard, E466, Standard practice for conduction force controlled constant amplitude axial fatigue test of metallic materials, Annual book 3 (2002).
[58] G.A. Holzapfel, G. Sommer, C.T. Gasser, P. Regitnig, Determination of layer-specific mechanical properties of human coronary arteries with nonatherosclerotic intimal thickening and related constitutive modeling, Am. J. Physiol.-Heart C 289 (5) (2005) H2048–H2058.
[59] F. Gervaso, C. Capelli, L. Petrini, S. Lattanzio, L. Di Virgilio, F. Migliavacca, On the effects of different strategies in modelling balloon-expandable stenting by means of finite element method, J. Biomech. 41 (6) (2008) 1206–1212.
[60] H. Hibbitt, B. Karlsson, P. Sorensen, Abaqus analysis user's manual version 6.10, Dassault Systèmes Simulia Corp, Providence, RI, USA, 2011.
[61] Anon, Abaqus analysis manual v6.10, Rhode Island, USA: DS SIMULIA, 2010.
[62] U. Food, D. Administration, Non-clinical tests and recommended labeling for intravascular stents and associated delivery systems: guidance for industry and FDA staff. US Department of Health and Human Services, Food and Drug Administration, Center for Devices and Radiological Health, 2005.
[63] ASTM-F2477-07, Standard test methods for in vitro pulsatile durability testing of vascular stents. Philadelphia, PA: American Society for Testing and Materials, 2007.